Final Draft

of the original manuscript

Zhang, Y.; Ren, J.; Zhang, W.:

Flocculation under the control of shear, concentration and stratification during tidal cycles.

In: Journal of Hydrology. Vol. 586 (2020) 124908.

First published online by Elsevier: 30.03.2020

https://dx.doi.org/10.1016/j.jhydrol.2020.124908

Flocculation under the control of shear, concentration and stratification during tidal cycles

Ying Zhang[a,b], Jie Ren[a,b,*], Wenyan Zhang[c]

[a]*Center for Coastal Ocean Science and Technology (CCOST), School of Marine Sciences, Sun Yat-sen University, Guangzhou 510275, China.*

[b]*Southern Marine Science and Engineering Guangdong Laboratory (Zhuhai)，Zhuhai 519000, China.*

[c]*Institute of Coastal Research, Helmholtz-Zentrum Geesthacht, Geesthacht, 21502, Germany*

Abstract

Tide-dominated estuaries are often characterized by a high variability of turbulent shear, suspended particulate matter (SPM) concentration and salinity, which imposes challenges for a comprehensive understanding of its mass transport including cohesive sediment dynamics. Here, a combined in situ and numerical study was undertaken to investigate the mechanism of flocculation during tidal cycles, with the aim to disentangle the impacts of turbulent shear, SPM concentration and salinity on flocs. Results show that microflocs (20-200 μm) dominate in the Pearl River Estuary and floc size variation is caused primarily by exchange between flocculi (4-20 μm) and microflocs. We also identified a critical shear rate (G* ≈ 5 /s) below which floc exchange occurs slowly. Above the threshold, the particle size distribution is left-skewed and clustered below 60 μm. Evolutions of flocs with different initial sizes synchronize gradually to adapt to the local

Abbreviations: ADCP, Acoustic Doppler Current Profiler; ADV, Acoustic Doppler Velocimeter; LISST, Laser In Situ Scattering and Transmissometry; OBS, Optical Backscatter Sensor; PSD, Particle Size Distributions; PSU, Practical Salinity Units

*Corresponding author at: School of Marine Sciences, Sun Yat-sen University, No. 135, Xingang Xi Road, Guangzhou 510275, China.

E-mail addresses: renjie@mail.sysu.edu.cn *(J. Ren).*

hydrological environment. The trends of floc size evolution and absolute net flocculation rates are similar among diverse tidal shear cycles. The reason can be attributed to the turbulent shear which enhances both aggregation and breakup processes, thereby limiting the floc size in a certain range. The higher the concentration, the larger both the particle size and the range of variation. In addition, results of numerical modelling reveal that the flocculation time for primary particles is inversely proportional to shear and concentration. A critical concentration ($C^* \approx 50$ mg/L), below which the impact of concentration on the equilibrium diameter of flocs is more than twice as strong as shear, whilst above which the equilibrium diameter is inversely proportional to the Kolmogorov microscale and weakly correlated to concentration, was also identified. Furthermore, halocline was found to increase vertical variation of flocs size, suggesting co-existence of different flocculation mechanisms across this layer.

Keywords: cohesive sediment; turbulence; equilibrium diameter; flocculation time; halocline

1. Introduction

Flocculation is an outcome of the simultaneous aggregation and break up of particles (Winterwerp and van Kesteren, 2004). A floc is a micro-ecosystem comprising a matrix of water, inorganic sediment particles and organic materials, with autonomous and interactive physical, chemical and biological functions and behaviors operating (Droppo, 2006). Floc size is a crucial parameter in determining the settling velocity and deposition rate of cohesive sediments (Droppo et al., 1998), and thus influences many practical applications, e.g., siltation in navigation channels, pollutants and nutrients transport, and morphologic evolution (Shen and Maa, 2015; Maggi, 2013). However, the complexity of coastal water mass transport, e.g. in tide-dominated estuaries characterized by simultaneously high variability of turbulent shear (G), SPM concentration (C) and salinity (S) in each tidal cycle, impedes a comprehensive understanding of flocculation mechanisms in natural waters (Thomas et al., 1999).

The impacts of two dominant factors, i.e. C and G, on flocculation characteristics such as floc size (D), rates of aggregation and breakup, equilibrium diameter (D_e, representing the floc size when aggregation and breakup are balanced) and flocculation time (T_f, representing the time required to attain D from an initial floc size under steady concentration and shear conditions) have yet to be quantified explicitly in situ (Winterwerp, 1998; Guo et al., 2017). It has been found that the evolution trend of is determined by . Flocs tend to grow when $D <$ and break when $D > D_e$. In addition, defines the maximal timescale of flocculation process (Winterwerp, 1998).

The impact of G on D has been explored extensively. In most previous studies, a critical shear rate representing an optimal condition for flocculation, below which the floc size increases with G

and above which the floc size declines with an increasing *G*, has been identified (Dyer, 1989; Mietta et al., 2009; Kumar et al., 2010). Value of this critical shear rate has been found to range around 15-40 /s (Manning and Dyer, 1999; Kumar et al., 2010; Sahin, 2014; zhang et al., 2019b). Large flocs (> 200 m) are supposed to form in slack water with reduced *G* (Guo et al., 2017). Accordingly, the Particle Size Distributions (PSDs) of flocs are skewed toward larger sizes under low turbulent shear, and vice versa (Lee et al., 2012). Moreover, is inversely proportional to the Kolmogorov microscale (Bowers et al., 2007; Cross et al., 2013). However, quantitative assessment of the impact of *G* on *D* in natural estuaries is still lacking because of the impact of various interacting environmental factors and forces which often lead to non-equilibrium status of *D* in response to changing *G* (Winterwerp, 1998).

Previous research indicates that the influence of *C* on *D* is not as straightforward as that proposed by classic aggregation theory, especially on the assumption that higher concentration increases floc size because of enhanced inter-particle collisions (Hill, 1998). For example, *C* is found to enhance flocculation when turbulence decreases (Guo et al., 2018), but has limited effect in promoting macrofloc (i.e., *D* > 200 μm) formation (Li et al., 2017). *D* responds quickly to a decrease in *C* (i.e., from 400 mg/L to 50 mg/L), but has a weak positive correlation with *C* when *G* is at a medium level (e.g. *G*=50/s) (Tran et al., 2018). These results suggest that the relationship between *C* and *D* is corrugated by *G*.

A further limitation in current understanding of flocculation is the relationship between , *C* and *G*. is usually used to estimate whether an equilibrium status could be achieved in a settling column (Maggi et al., 2002). The measured maximum floc size could be locally maintained only if exceeds the floc residence time (Cuthbertson et al., 2010). An increase in *G* is supposed to shorten through increasing both aggregation and breakup rates (Mietta et al., 2009; He et al., 2018). An analytical solution of can be obtained based on the Winterwerp flocculation model (Winterwerp 1998, 2002) by relating to , *C* and *G*. However, the model has been further developed to be more applicable (Kuprenas et al., 2018). Specifically, a more precise formulation of is desirable.

Besides a dominant control by *C* and *G*, the impact of salinity including salinity-induced stratification such as front or halocline on flocculation could not be neglected in estuarine environments (Ren and Wu, 2014). An increase in salinity is supposed to enhance flocculation as salt would decrease the particles' surface charge (Mietta et al., 2009). However, based on in situ observations, contradictory results have been derived with regard to the impact of an increasing salinity on floc size (Burt, 1986; Eisma et al. 1991; van Leussen, 1999). A consensus about the role of salinity is that there exists an optimum salinity for flocculation. However, its value is dependent on the specific environmental and SPM lithologic configuration (Shen and Maa, 2016; Guo et al., 2017).

It is difficult to measure the exact rates of simultaneous aggregation and breakup and to investigate flocculation mechanism in situ due to constantly changing *C* and/or *G* and/or *S*. Instead, these rates could be estimated by numerical models that fit observed distribution of flocs, and then the model could help predict transport and fate of fine-grained suspended cohesive sediments (Shen and Maa, 2015, 2016). Thus, development of robust numerical models which could resolve the complex interactions between flocculation and its controlling factors is of critical importance. In general, three types of flocculation model exist. The first is based on the extended Lattice Boltzmann Model, which is able to predict a full spectrum of flocs properties such as PSDs and settling velocities but on the other hand is highly expensive in terms of computational cost (Zhang et al., 2013). The second type is the so-called Population Balance Modeling which represents PSDs with two or multiple size groups/classes (Maggi et al., 2007; Lee et al., 2011, 2014; Shen and Maa, 2015, 2016; Shen et al., 2018a). The third type refers to the Winterwerp flocculation model, which traces the evolution of a characteristic floc size and describes the relevant aggregation and breakup processes. The Winterwerp flocculation model is widely used because of its high computational efficiency and easy integration into hydrodynamics models (Winterwerp, 1998, 2002; Winterwerp and Kesteren, 2004; Kuprenas et al., 2018).

Based on in situ measurements in the Pearl River Estuary and numerical modelling results, this study aims to further advance the understanding of flocculation processes by (1) modelling the flocculation process in response to changing *C* and *G* in tidal cycle, (2) assessing the quantitative impact of *C* and *G* on the equilibrium diameter and flocculation time , exploring (3) the response of floc size *D*, aggregation and breakup rates to initial particle diameter , *C*, and *G*, and (4) the impact of salinity-induced stratification (halocline) on flocculation.

2. Materials and Methods

2.1. Regional Setting and field measurements

The study area is located in the Pearl River Estuary situated in south China (Fig. 1). Hydrodynamics of this area is mainly controlled by semidiurnal tides with obvious salinity, velocity, and turbidity cycles. The mean annual loads of freshwater and riverine sediment are approximately 2.86×10^{11} m^3 and 3.04×10^7 t, respectively (Zhang et al., 2019a). Two sites with contrasting salinity conditions, namely B1 which is affected mainly by freshwater flow and B2 which is featured by periodic salt water intrusion following a tidal cycle, were selected to investigate flocculation processes (Fig. 1).

Field work recording PSDs, turbulence, turbidity, and salinity was conducted continuously covering two full semi-diurnal tides between August 24–25, 2018 and August 25–26, 2018 at the two sites, respectively. In situ PSDs of volume-equivalent spherical particles in 36 logarithmically spaced size groups over the range 1–500 μm were measured using the LISST-200X (Laser In Situ Scattering and Transmissiometry) instrument (Agrawal and Pottsmith, 2000), which is valid for SPM concentrations from <20mg/L to 1000 mg/L (Fettweis et al., 2006; Guo et al., 2017). The salinity, temperature, and turbidity were measured using an OBS-3A (Optical Backscatterance Sensor). The device was connected online so that the depths of interest (e.g., surface, middle and bottom layers or thin layer: boundary layer, halocline, thermocline) can be located by real-time transmitted data. The LISST-200X and OBS-3A were installed in a steel frame that was deployed at an hourly interval. In each deployment it was firstly lowered from the water surface to the bottom in a steady speed of ~0.1m/s. Then, the device stayed in the bottom, middle (where the halocline was located) and surface layers by turn where they remained for approximately 5 min each with sampling frequency of 1 Hz. Meanwhile water samples were collected and filtered by preweighed filters for calibration of turbidity and SPM concentration values. Bottom sediment samples were also collected for analysis of the size of primary particles using a Malvern Mastersizer 3000, which covers a size range of 0.01–3500 μm.

In addition, an Acoustic Doppler Velocimeter (ADV) and 5-beam Acoustic Doppler Current Profiler (ADCP) were mounted on a benthic tripod and deployed at each site. Turbulence data were collected by the ADV (64 Hz) located at 0.55 m above the bed. The vertical current structure was measured by the upward-looking ADCP which operated at 8 Hz in twelve bins (50-cm interval) with 5-min bursts in every 10 min.

2.2. Data Processing

2.2.1. LISST Data

Four steps were performed to obtain the PSD of each layer. These include 1) data inversion, 2) quality control, 3) spike removal, and 4) ensemble averaging. In the first step, small-angle scattering data were inverted into PSD data using a Matlab inversion script (http://www.SequoiaSci.com). In the step of quality control, optical transmission within a range of 0.15–0.98 was considered to indicate good quality data (Agrawal and Pottsmith, 2000). The third step, spike removal, was essential to eliminate both the effects of short-term variations and the influence of advection, vertical sediment transport, and outliers of the PSDs (Mikkelsen and Pejrup, 2001). We applied the method of local outlier factor detection by Breunig et al. (2000) which is implemented in Python to remove spikes of particle size from the time series of the median particle diameter (D_{50}). After this step, covariance of the ensemble D_{50} was reduced significantly (e.g., to 1/2 of the pre-processing value in surface layer at site B1). In the final step, the PSDs of each layer were averaged for each hourly internal to produce representative PSDs.

2.2.2. Decomposition of Multimodal PSDs

Generally, the PSDs of flocs in a coastal zone can be decomposed into four lognormal size classes to represent primary particles (0–4μm), flocculi (4–20μm), microflocs (20-200μm), and macroflocs (200-500μm) (Lee et al., 2012; Hussein et al., 2005; Mäkelä et al., 2000; Whitey, 2007) given by:

$$\frac{dV}{dD} = \sum_{i=1}^{4} \frac{\overline{V_i}}{\sqrt{2\pi}\ln(\sigma_i)} exp\left[-\frac{1}{2}\left(\frac{\ln(D/\overline{D_i})}{\ln(\sigma_i)}\right)^2\right], \quad (1)$$

where V, and D are the volumetric concentration and diameter of each size interval of the LISST-200X measured PSDs, respectively, dV/dD is the volumetric fraction normalized by the width of the size interval that is used for curve fitting to a lognormal distribution (Hinds, 1999), and $\overline{D_i}$, σ_i, and $\overline{V_i}$ (Eq. (1)) are the representative size, standard deviation, and volumetric concentration, respectively, of the i-th lognormal PSD (i =1, 2, 3, 4). The mean diameters of the four size classes were derived as curve fitting parameters based on observation. Here, σ_i was limited to <2.5 to prevent unrealistically wide PSDs (Fettweis et al., 2012). A mean value of $\sigma_i = 1.63$ was obtained in our observation. The curve fitting tool implemented in Python (http://www.scipy.org/) was used to determine the best fit to a measured PSD, i.e., the minimum error between the simulated and measured PSDs (Lee et al., 2012). The quality of the curve fitting analysis was monitored with absolute percentage error, defined as the ratio between the sum of errors and experimental data.

2.2.3. Turbulence data

Turbulent shear rate (G) is defined as $G = \nu/\eta^2 = \sqrt{\epsilon/\nu}$ (/s), where ν is the kinematic viscosity of the fluid, η is the Kolmogorov microscale and ϵ is the mean turbulent energy dissipation rate. G was estimated from the high-frequency velocity data recorded by the ADV.

The ADV-derived raw data requires preprocessing before turbulent parameters can be estimated. A robust nonparametric technique that can identify outliers (Thompson, 1985; Lanzante, 1996) was used to remove spikes from the pulse velocity time series. Afterwards, the turbulence kinetic energy (TKE) spectra method (Guerra and Thomson, 2017) was applied to estimate ϵ:

$$S_w(f) = \alpha\epsilon^{2/3}f^{-5/3}(\frac{\overline{u}}{2\pi})^{2/3}, \qquad (2)$$

where S_w is the TKE spectra, f is the frequency, α is a constant (=0.69) (Sreenivasan, 1995), and

$\bar{u}$ is the mean along-channel velocity.

The TKE spectra method is based on the Kolmogorov hypothesis, i.e., there exists a range of turbulent length scales within the isotropic turbulence energy cascade, known as the inertial subrange, in which energy transfer is determined solely by the dissipation rate (Kolmogorov, 1941; Pope, 2000). However, the inertial subrange is variable due to changes in the hydrological factors. This imposes a challenge to solving the dissipation rate. To derive a precise inertial subrange, a three-step procedure was applied in this study.

Firstly, each estimated spectrum was multiplied by $f^{5/3}$ to obtain a compensated spectrum, which should be horizontal (flat) in the presence of an inertial subrange. The dissipation rate was estimated by solving Eq. (3):

$$\overline{S_w(f) f^{5/3}|_{f1}^{f2}} = \alpha \epsilon^{2/3} (\bar{u}/2\pi)^{2/3}, \qquad (3)$$

where f_1 and f_2 indicate the lower and upper frequency limit of the compensated spectrum, respectively (Guerra and Thomson, 2017). The range of frequencies varies for different mean flows between $2<f<10$Hz in our observation.

Secondly, the frequency range (e.g., 2-10 Hz) was divided into intervals (e.g., 0.2 Hz), so that the subrange collection was obtained by permutation and combination. The frequency band of each subrange was required to be no less than 2 Hz to provide sufficient integral spectrum data.

The final step is to search the optimal subrange. Criteria for defining the best subrange include: (a) the error between the compensated spectrum and its robust regression is sufficiently small (e.g., <30% percentile); (b) the slope of the robust regression is sufficiently close to zero (e.g., <10% percentile); (c) afterwards, sufficient integral spectrum data remain for the calculation. (e.g., >50% percentile); and (d) then the slope of the robust regression is the closest to zero.

2.3. Numerical modelling of flocculation

The Winterwerp (1998) model (referred to W98 hereafter) is a simple Lagrangian-type floc growth equation used to predict the temporal evolution of a single characteristic floc size. It reflects how factors such as shear, concentration, floc structure, and the inherited floc size act on the aggregation and breakup rates. Specifically, it is a rate equation for an average floc size (D) expressed as:

$$\frac{dD}{dt} = A - B, \quad (4)$$

where A and B are the aggregation and breakup kernels, respectively, expressed in dimensions of [L/t]. A and B are calculated by:

$$A = \frac{k_A{}'}{n_f} \frac{{D_P}^{n_f - 3}}{\rho_s} GCD^{4-n_f},$$

$$B = \frac{k_B{}'}{n_f} DG \left(\frac{D - D_P}{D_P}\right)^p \left(\frac{\tau_t}{\tau_y}\right)^q, \quad (5)$$

where D_p is the size of the primary particles, n_f is the floc fractal dimension, ρ_s is the density of the unflocculated sediment, and p and q are nondimensional power coefficients in the floc erosion kernel. $k_A{}'$ is a dimensionless aggregation coefficient, defined as $k_A{}' = \frac{3 e_c \pi e_d}{2 f_s}$, where f_s is a floc shape factor, and e_c and e_d are efficiency parameters for coagulation and diffusion, respectively. e_c is an empirical parameter related to the physicochemical properties of the sediment and the water, as well as the organic compounds within the sediment (Van Leussen, 1994). $k_B{}'$ is an empirical coefficient of floc breakup efficiency. τ_t is the turbulence-induced stress on the floc and τ_y is the strength of the floc. They are calculated by:

$$\tau_t = \mu G,$$

$$\tau_y = \frac{F_y}{D^2}, \quad (6)$$

where μ is the dynamic viscosity of the fluid and F_y is the floc yield strength in dimensions of force.

Winterwerp (1998) proposed that $p = 3 - n_f$, based on the assumptions that $D_p \ll D_e$ and $D_e \propto 1/\sqrt{G}$ (Bowers et al., 2007; Cross et al., 2013). $q = 0.5$ is adopted to satisfy that settling velocity $\omega \propto D$. Uncertainty in the coefficients $k_A{}'$ and $k_B{}'$ related to the SPM concentration limits the use of the W98 model for predictive modeling. As an alternative, Kuprenas et al. (2018) modified the coefficient q of the W98 floc breakup rate kernel (referred to K18 hereafter) as follows:

$$q = c_1 + c_2 \frac{D}{\eta}, \quad (7)$$

where c_1 and c_2 are constant coefficients. This simple modification limits the size of the floc to the Kolmogorov microscale (η), thereby improving the time-dependent solution behavior without requiring recalibration coefficients for each change of concentration.

The key state variables in K18 model include the particle size, the mass SPM concentration and the turbulent shear. In this study, time series of these variables derived from field observation were fed into the model to evaluate the flocculation process. The parameters setting used to explore the PSDs evolution in tidal cycles was as follows: n_f = 2, F_y = 1E−10 N, ρ_s = 2650 kg/m^3, p = 3 − n_f, $c_1 = 0.5$, $c_1 = 1.5$, and D_P= 5 μm according to the Malvern measurements (Zhang et al., 2019b), the initial particle size D_0 was set to the size of the measured floc at the beginning ($t = 1$), μ was calculated based on in situ temperature and salinity data, G was derived from the ADV, and C was determined from OBS after calibration. More details about the choice of these parameters and its sensitivity analysis could be found in Kuprenas et al. (2018).

3. Results

3.1. Hydrodynamic conditions

The field survey sites B1 and B2 (Fig. 1) were in shallow water with average depth of approximately 3.3 and 5.0 m and mean SPM concentration of approximately 30 and 40 mg/L, respectively (Fig. 2). The semi-diurnal tides were asymmetric and ebb-dominant. The maximum vertically averaged ebb flow velocity at B1 and B2 was 0.51 and 1.13 m/s, respectively (Fig. 2a and 2d).

At site B1, the variations of channel velocity, salinity, and mass concentration were almost consistent throughout the entire water column (Fig. 2a–c). Fresh water dominated here with salinity mostly <2 Practical Salinity Units (PSU). However, the arrival of a density front at high water of the flood tide (at 22 hr) caused an abrupt change characterized by a drastic rise of salinity up to 5 PSU (Fig. 2b) and a large vertical gradient of SPM concentration near the seabed at this site (Fig. 2c).

Site B2 was further offshore and the water mass there was notably different from site B1. Site B2 was dominated by saline water (20 ± 4 PSU) characterized by a halocline near the surface (Fig. 2e). The vertical structure of velocity varied widely, e.g., strong currents were confined mainly at the surface but sometimes penetrated into the middle layer (Fig. 2d). It is worth to note that an exceptionally high SPM concentration event (> 200 mg/L) occurred at 6 hr during the monitoring period near the seabed at this site (Fig. 2f).

3.2. PSD variation

3.2.1. Vertical Structure of PSDs at High/Low Shear Rate

Profiles of high shear (Fig. 3a) at 4 hr (referred to HS hereafter) and low shear (Fig. 3b) at 8 hr (referred to LS hereafter) at site B1 with the same salinity structure and similar concentration range were selected for analysis. The vertical average diameter of HS (37 μm) was significantly smaller than LS (60 μm). The PSD of HS was centered around 22 μm with significant positive skewness, whereas that of LS was centered around 66 μm with slightly negative skewness. Microflocs with a mean diameter of 31 μm dominated in HS, accounting for 74.2% of the total volume of particles, while macroflocs with a mean diameter of 370 μm accounted for only 0.9% (Fig. 3a). In LS, the fractions of microflocs and macroflocs were 56.4% and 11.8% with mean diameters of 88.6 and 376 μm, respectively (Fig. 3b). These findings confirm that particle size is generally smaller in stronger shear environment. In addition, floc size increased slightly from the surface towards the bottom layer. The mean diameter of the microflocs in the surface, middle, and bottom layers was 29.6, 28.0, and 35.6 μm, respectively, in HS and 71.6, 82.5, and 111.9 μm, respectively, in LS. Furthermore, the transformations of the PSDs in the vertical axis were not as gradual and smooth as turbidity or salinity (Fig. 3). On the contrary, they were characterized by abrupt and jagged changes (Fig. 3b) due to the reason that the transformation of floc size is caused by particle collisions rather than by diffusive movements. Strong correlation was found between mass concentration and volume concentration with r = 0.74 in HS and 0.68 in LS. This indicated that the density of flocs was vertically uniform at site B1.

3.2.2. PSDs in Different Layers at Characteristic Times

In peak flood (at 11 hr) and ebb (at 4 hr) flows, the vertical mean diameters were 37 ± 6 and 25 ± 4 μm, respectively (Fig. 4c and 4g). The PSDs of the three layers (surface, middle, and bottom) were similar in both flood and ebb peak flows, e.g., with primary particles, flocculi, microflocs, and macroflocs accounting for 6.4(±0.5)%, 26(±6)%, 67(±6)%, and 0.75(±0.25)%, respectively. However, the mean diameter in slack waters was notably larger than that in peak flows, with values of 70 ± 37 and 40 ± 12 μm in the flood-to-ebb slack water (at 13 hr) and ebb-to-flood slack water (at 9 hr), respectively (Fig. 4e and 4i). In addition, PSD in slack waters was broader, especially in the surface layer which exhibited a dual-peak concentrated around 5 and 66 μm. These results indicate that flocculation prevails over deflocculation in a low shear environment (i.e. $G \approx 1$/s in slack water), and vice versa.

The PSDs at site B2 in the middle and bottom layers showed similar patterns with site B1, but differed significantly in the surface layer. During the peak flow periods, the portion of macroflocs in the surface layer at B2 accounted for 25% and 65% for the flood (at 16 hr) and ebb (at 25 hr), respectively (Fig. 4d and 4h), while during slack water a right-skewed PSD appeared there. Sediment resuspension was enhanced during the ebb peak flow (at 25 hr) with near-surface concentration up to 36 mg/L, compared to the values during the slack waters (both around 22 mg/L). The short-lasting but intense resuspension at 6hr induced not only an increase of SPM concentration but also a drastic increase of the portion of macroflocs (Fig. 5f and 5g). In addition, a strong halocline occurred during the flood peak flow (at 16 hr), followed by a dual-peaked PSD in the surface layer. These findings indicate that flocculation was enhanced by increased SPM concentration and the existence of a halocline.

It is interesting to note that the mean diameters of the entire water column at the two sites (B1 and B2) were almost the same (~40 μm) (Fig. 4a and 4b) over the monitored tidal cycles, despite of different PSDs with more macroflocs (22%) at site B2 than site B1 (4%). The significant differences in the PSDs between the two sites highlight the complexity of the spatial variation of flocculation in response to various environmental factors.

3.2.3. PSD Evolution in a Tidal Cycle

The PSDs in the bottom layer were selected for analysis, because the hydrological conditions of this layer were more consistent with that of the benthic tripod. Comparison of the PSDs in the bottom layer at sites B1 and B2 (Fig. 5a and 5f) in relation to turbulent shear G revealed that flocs broke up quickly in high shear conditions (G > 5/s) and concentrated at sizes below 60 μm (Fig. 5d and 5i). Conversely, the PSDs were skewed toward larger sizes and particles aggregated more to form macroflocs at low shear conditions (G < 5/s). The PSDs in the bottom layer were decomposed into lognormal distributions of primary particles, flocculi, microflocs, and macroflocs (Fig. 5b and 5g) to investigate the multimodality. Primary particles, flocculi, microflocs, and macroflocs accounted for 5%, 23.7%, 63.2%, and 8.1%, respectively, at site B1 and 8.5%, 35.6%, 54.0%, and 1.9%, respectively, at site B2 when averaged over two monitored tidal cycles. Microflocs dominated at both sites in the Pearl River Estuary and the variation of PSDs was caused mainly by constant flocculi–microfloc exchange. The fraction of each size class was steady during low turbulent shear conditions (G < 5/s), but readjustment of the PSDs with frequent exchange between neighboring classes occurred during high turbulent shear (G > 5/s). These results suggest the existence of a critical shear rate (G^*) below which the rates of breakup and aggregation are comparable resulting in a slow exchange between neighboring classes, and above which the breakup rate is accelerated rapidly leading to a left-skewed PSD with sizes mostly below 60 μm. The value of G^* depends on the constitution of the flocs. For sites B1 and B2 which were both in shallow water, a value of $G^* \approx 5$ /s was identified from the field data.

3.2.4. Numerical modelling

Particle size is determined by its value in the previous moment and the current change rate influenced by interior and environmental factors, i.e., $D_t = D_{t-1} + dD/dt$. Our field observation shows nonlinear relationships between the particle size and the influencing factors. Numerical models were used to further unravel the relationships.

By using K18 to estimate the impacts of mass concentration (C) and turbulent shear rate (G) on flocculation based on the time series of field data, we found that values of $k_A{}' = 0.45$ (0.55) and $k_B{}' =$ 3.0E−5 (5.0E−5) worked reasonably well for site B1 (B2) most of the time (Fig. 5c and 5h). These values are close to those derived in previous research, e.g., $k_A{}' \approx 0.15$ and $k_B{}' = O\{10^{-5}\}$ by Winterwerp (1998), and $k_A{}' = 0.5$ and $k_B{}' =$ 5.0E−6 by Kuprenas et al. (2018). The model was able to predict the size of flocs, track its transition point, and capture the range of floc size variation (Fig. 5c and 5h), with r = 0.74 (0.72) and RMSE = 17 (12) μm for site B1 (before 22 hr) (B2), despite of some bias. This model shows a reasonable performance when G and C changes, considering the variation of G (Fig. 5d and 5i) and C (Fig. 5e and 5j) were inconsistency in this case.

The mismatch at site B1 when front occurred (after 22 hr) is partly attributed to changing water properties that could have affected $k_A{}'$ via e_c and $k_B{}'$. The mismatch at site B2 around 6 hr is partly attributed to small particles from resuspension or advection. Besides, the other three factors could also cause some bias: (1) simplified model parameters; (2) relatively low resolution of the data because of the limited sampling rate; (3) sediment trapping by the halocline which was not considered in the model.

The overall good agreement between simulation results and field data provides us a strong argument that the model has reliably reproduced a suite of scenarios of flocculation and that the results can thus be interpreted in further detail to derive insights into the impacts of G and C on flocculation.

4. Discussion

4.1. Floc Size Evolution

The effects of initial particle size D_0, shear rate G, and concentration C on floc size evolution were investigated respectively by using the control variable method (i.e. only one factor was changed at a time) based on the combination of data from site B1 and numerical study.

Five initial floc sizes, namely $0.25D_0$, $0.5D_0$, D_0, $1.5D_0$ and $2.5D_0$ where D_0= 45 μm, were defined in the first set of model test. Results show that the floc size evolution converged to D_0 at around 3.8 hr for initial sizes larger than D_0,(Fig. 6a). Evolution of the $0.5D_0$ particle size (23 μm) converged to the larger size groups later at 10 hr, which is close to one tidal cycle. However, the smallest particles ($0.25D_0$ =11 μm) appear to grow continuously and approach the curves of other size groups not earlier than at 22hr (~ two tidal cycles). These results reveal that particles with different size would be gradually assimilated; that is, only particles of a certain size could be maintained under certain circumstances. But the assimilation rate depends on the initial particle size, i.e., higher rate with larger particles and vice visa.

The same scaling factors were applied to the shear rate in a second set of model test. Results show that the larger the shear, the smaller the particle size is (Fig. 6b). It is interesting to note that the trends of floc size evolution after 2.7 hr are consistent in all shear rates except in the lowest case (0.25*G*). Their sizes range of variation increase in sequence of 24, 26, 29, and 37 μm (multiplied with 0.5, 1.0, 1.5, and 2.5) respectively. The particle size in lowest *G* deviate from others by showing a quasi-equilibrium at around 94 μm after 14 hr. A slightly decreased shear rate (0.5*G*) results in an increase of particle size by 16.7% compared to the reference result of *G*, with mean values from 72 μm to 84 μm. In contrast, a further enhancement of the shear rate to 2.5*G* led to a decrease of particle size by 25.3% to 53.8 μm compared to the reference result. These outcomes explain the results in Section 3.2.1 that the average diameter of flocs in HS (37 μm) was significantly smaller than that in LS. Similar result was derived by Guo et al. (2017) who found that particle diameter in a spring tide with stronger shear is much smaller than in a neap tide.

In a third set of model test the impact of SPM concentration was investigated. We found that higher concentrations lead to larger particle sizes and a greater range of variation (Fig. 6c). In high shear conditions (e.g., *G* = 8/s at 10hr), particle size becomes almost uniform for diverse concentration, which indicates a dominant control of high shear on floc size. In the case of high concentration (2.5*C*), the maximum floc size is ~515 μm when *G* is low (i.e., *G* = 1/s at 14 hr), exceeding the upper limit of the LISST measurement range, which explains the warping tail phenomenon observed in regions of high turbidity. If concentration is low (e.g. in cases of 0.25C and 0.5C), flocs would grow slowly and their size would vary in a small range from the initial size. This explains a limited floc development in open seas with clear water as well as provides the justification for a larger span of floc size in a spring tide with higher concentration than that in a neap tide reported by Guo et al. (2017).

It is interesting to note that the asymmetrical fluctuations of floc size become more apparent with a decrease of both shear (Fig. 6b) and concentration (Fig. 6c), i.e., longer time is needed to reach the maximum floc size in a tidal cycle in case of low shear and concentration. This might help predict the time with maximum floc size when upstream runoff and sediment change or when shear changes in a neap–spring tidal cycle.

4.2. Aggregation and Breakup Rate in Different Cases

The exact values of *A* and *B* in Eq. (5) determine the flocculation process. For site B1 (Fig. 6g), the maximum absolute values of aggregation and breakup rates were both 6.0×10^{-2} μm/s, and the net rate dD/dt ranged from -1.77×10^{-2} to 1.07×10^{-2} μm/s with a mean absolute value of 2.8×10^{-3} μm/s in the two tidal cycles.

In case of small initial floc size ($0.25D_0$, Fig. 6d), the terms A and B were around 1.53×10^{-5} and -2.3×10^{-6} μm/s, respectively, with the net rate around only 1.3×10^{-5} μm/s at first, and it persisted for 2.46 h. For the high D_0 case ($2.5D_0$, Fig. 6j), the rate of floc breakup was greater than the rate of aggregation; the net rate even reached -1.9×10^{-2} μm/s at first because B is more sensitive to particle size than A. Comparison of the two case reveals that smaller flocs are likely to remain unchanged for several hours because of the low aggregation and breakup rates, in contrast, larger flocs breaks up freely. It also explains that larger particles can be more easily assimilated (Fig. 6a).

For high shear conditions (1.5G and 2.5G), the terms A and B were within 1.58 (±61%) × 10^{-2} and −1.07 (±12%) × 10^{-3} μm/s, respectively (Fig. 6h and 6k). However, the resultant net rates were confined within a small range of 2.74 (±2.2%) × 10^{-3} μm/s. Shear enhances both aggregation and breakup processes, thereby limiting the net rates and floc size in a certain range. It explains that the trends of floc size evolution are consistent in diverse shear rates (Fig. 6b). In low shear condition (0.25G), the mean values of A and B were 2.46×10^{-3} and -1.51×10^{-3} μm/s, respectively, being only 1/4 and 1/6 of the values in original shear (G) condition (Fig. 6g). These results suggest that a decrease of shear would lead to decrease in both aggregation and breakup rates. A continuous growth of floc size might be attributed to a larger deduction of term B (by 5/6) than that of term A (by 3/4) (Fig. 6b).

Furthermore, the maximum absolute values of aggregation and breakup rates were both in $O\{10^{-3}\}$, with a mean value of the net rate of -2.67×10^{-4} μm/s for low concentration condition (0.25C, Fig. 6f). However, these rates were notably different for high concentrations (2.5C, Fig. 6l). The maximum and mean values of aggregation and breakup rates were almost two orders of magnitudes higher than the low concentration case and characterized by significant fluctuations causing occasionally drastic change of floc size (Fig. 6c). The absolute value of net rate in high concentration (2.5C) condition was 1.53×10^{-2} μm/s, approximately 55 times larger than the low concentration (0.25C) condition (Fig. 6f). This also explains the larger variation of floc size in higher concentration condition (Fig. 6c).

4.3. Impact of Shear and Concentration on Equilibrium Diameter and Flocculation Time

In the simplified W98 model, A=B leads to the equilibrium diameter $D_e = D_p + \frac{k_A C}{k_B \sqrt{G}}$, where $k_A = \frac{1}{2}\frac{k_A{}'}{\rho_s D_P}$ and $k_B = \frac{k_B{}'}{2}(\frac{\mu}{F_y})^{1/2}$. This relationship indicates that the impact of concentration C on D_e is larger than that of shear G and that D_e increases as C increases. However, this disagrees with existing observations (Cuthbertson et al., 2010; Guo et al., 2018; Tran et al., 2018). In K18, assuming that $D_P \ll D$ and $n_f = 2$, A=B leads to:

$$K_a \mathrm{C} \approx (K_b G D_e{}^2)^{\frac{1}{2}+K_c\left(G D_e{}^2\right)^{\frac{1}{2}}}, \quad (8)$$

where $K_a = \frac{k_A{}'}{\rho_s k_B{}'}$, $K_b = \frac{\mu}{F_y}$, and $K_c = \frac{5}{2}\nu^{-1/2}$. It is difficult to separate out D_e in this formulation because of the modified q (Eq. (7)) in Eq. (5). However, numerical simulation results (Fig. 7a) based on data from site B1 indicate that D_e is dependent on shear and concentration. Results also suggest the existence of a critical concentration (C^*) below which the impact of concentration on D_e is stronger than shear, while above which D_e is inversely proportional to the Kolmogorov microscale and weakly correlated to concentration. Similar patterns were also obtained for different values of $k_A{}'$ and $k_B{}'$, suggesting the wide existence of the empirical formulation

$D_e = \frac{KC^{c1}}{G^{c2}}$. The value of C^* depends on the constitution of flocs and environmental factors (e.g., organic matter, PH). For site B1, a value of $C^* \approx$ 50 mg/L was found to work reasonably well (Fig. 7a). By using curve fitting tools, the best values of $c1$, $c2$ and K in the empirical formulation $D_e = \frac{KC^{c1}}{G^{c2}}$ were obtained. For $C < C^*$, $c1 = 0.72, c2 = 0.32, K = 10^{-3}$; for $C > C^*$, $c1 = 0.13, c2 = 0.5, K = 10^{-3.27}$. For $C < C^*$, the impact of concentration on flocculation is more than twice as strong as shear. However, floc size is limited gradually by shear as concentration increases, consistent with $D_e \propto \eta$, and the effect of shear on D_e becomes more than three times as strong as concentration when $C < C^*$. This finding agrees with the experimental measurements of Tran et al. (2018), showing that D_e has weak dependence on concentration when $C \geq 50$ mg/L.

The concise expression $CGT_f = 1.2 \times 10^4$ for $D_0 = D_p$ is consistent with the model results based on site B1 data when the concentration is not too low (i.e., $C \geq 10$ mg/L) and $D_e > 10$ µm (Fig. 7b). Similar patterns were also obtained for different values of $k_A{}'$ and $k_B{}'$, which indicates that $T_f \propto 1/(CG)$ may apply widely. This relationship provides a simple way to estimate whether the quasi-equilibrium state could be achieved in both lab experiment and field and thus sheds light on evaluation of the floc status. As Winterwerp (1998) showed, $T_f \approx 2T'$ when $D_e \ll D_0$, and $T_f \approx T' \frac{D_e}{D_0}$ when $D_e \gg D_0$, where T' is a timescale parameter defined as $T' = \frac{1}{k_B G^{3/2} {D_e}^2}$. The T_f in the former case is far less than the latter because $\frac{D_e}{D_0} \gg 2$. This accounts for the asymmetry of the aggregation and breakup rates of the particles (Fig. 6b and 6c), i.e., particle size decreases more rapidly than it increases, especially for larger particles. For $D_e \gg D_0$, $D_e = D_p + \frac{k_A C}{k_B \sqrt{G}} \approx \frac{k_A C}{k_B \sqrt{G}}$ in case of sufficiently small D_p, we obtain $CGT_f \approx \frac{1}{k_A D_0} \approx 3.55 \times 10^4$, which is larger than the results of the K18 model (i.e., $CGT_f = 1.2 \times 10^4$). The reason for this difference is that the particle size in K18 is limited to the Kolmogorov microscale η (see Eq. (7)), thus, the time required to reach equilibrium status decreases. Furthermore, in the Pearl River Estuary, D_e and T_f vary considerably from 10–290 μm and from 6–200 hr, respectively, accounting for non-equilibrium status commonly found in the field.

4.4. Impact of Salinity on Vertical Distribution of Floc Size

There were large differences between site B1 and B2 in the hydrological background (see Section 3.1), especially in the salinity structure (Fig. 2b and 2e). Comparison of the median diameter between the two sites in the entire water column and upper and lower layers relative to halocline (Fig. 8) revealed that salinity could increase the vertical variation of floc size. In site B1 which is dominated by fresh water, strong correlation of floc size was found among the three layers, i.e., 0.96 and 0.85 between the entire water column and the upper and lower layers respectively. In site B2 characterized by stratified water with a halocline (Fig. 2e), the mean diameter of flocs in the entire water column showed significant positive correlation with the upper layer (r= 0.78), but negative correlation with the lower layer (r= -0.25). Another remarkable difference is the particle size between the surface and bottom layers. The mean floc diameter in the upper layer (43 μm) was smaller than in the lower layer (56 μm) at site B1, while the situation at Site B2 was the opposite, with much larger particles in the upper layer (90 μm) than in the lower layer (39 μm). This distinct pattern indicates that the halocline forms a “barrier” between freshwater in the surface and saltwater in the bottom, and hinders vertical exchange of flocs. At site B2, the vertical average standard deviations of floc size were 45 and 42 μm in the entire water column and the upper layer, respectively, being much larger than that in the lower layer (13 μm). In contrast, floc size varied a little with standard deviations of 18, 15 and 11 μm in the three layers at site B1. This reveals that the flocs in the upper layer were trapped by the halocline at site B2.

The distinct patterns of flocculation above and below the halocline with very limited exchange implies that flocculation modeling in stratified estuarine waters can be simplified into two layers with the boundary at the halocline.

4.5. Perspectives of future work

This study proved the general validity of the modified Winterwerp model (Kuprenas et al., 2018) and its use in understanding flocculation performance in an estuary (the Pearl River Estuary). However, performance of this model is also likely to be affected by changes in water properties and resuspension of large numbers of small particles from the bed. Besides the factors discussed above (i.e., *G*, *C*, and *S*), a wide range of physical and biogeochemical factors (e.g., organic matter content, PH value and ionic strength) are also found to have considerable impacts on flocculation (e.g. Maggi, 2009; Nguyen et al., 2018; Shen et al., 2018b, c; Lai et al., 2018). However, the nonlinear relationships among these variables increase the complexity of depicting in situ flocculation. In addition to further development of mechanistic models for better presenting flocculation dynamics under the control of various physical and biogeochemical factors, big data-driven approaches may provide a promising alternative. Artificial Intelligence (AI) approaches have proven to be capable to recognize complex and nonlinear relationships among large number of variables, and therefore might provide a new way of flocculation modeling. So far AI has been successfully used to predict water quality (Shamshirband et al., 2019) and assessment of suspended sediment load in estuaries and coastal waters (Olyaie at al., 2015).

5. Conclusions

This study investigated flocculation in a tide-dominated estuary based on in situ observations and numerical modelling with the aim to derive further insights into flocculation processes controlled by varying shear, concentration and salinity conditions. Based on the results, the following conclusions are drawn.

1. In the Pearl River Estuary, microflocs generally dominate and the variation of the PSDs is caused mainly by constant exchange between flocculi and microflocs. A critical shear rate ($G^* \approx 5$ /s), below which floc exchange occurs slowly and above which the PSDs become left-skewed and clustered below 60 μm, is identified for the study sites. On the other hand, the trends of floc size evolution are similar among diverse tidal shear cycles because of the limitation of shear on particle size.
2. The net flocculation rate is higher when the initial floc size is larger. However, this applies only to the initial phase and the rates become gradually synchronous among cases of different initial floc size.
3. Flocculation is facilitated by increase of SPM concentration. The increasing rate of the net flocculation rate however is one order of magnitude larger than that of SPM concentration.
4. A critical concentration ($C^* \approx 50$ mg/L), below which the impact of concentration on the equilibrium diameter of flocs (D_e) is more than twice as strong as shear, while above which D_e is inversely proportional to the Kolmogorov microscale η and weakly correlated to concentration, was identified for area dominated by fresh water flow. In other words, the impact of concentration/shear on D_e decreases/increases as concentration increases, and D_e is inversely proportional to η in case of high concentration (> 50 mg/L).
5. The time required to achieve D_e from an initial floc size D_0, namely T_f, is dependent on the SPM concentration (C) and the turbulent shear (G) through a relationship $T_f \propto 1/(CG)$. In shallow waters dominated by barotropic flow (i.e. vertically homogeneous) and medium

SPM concentration level (C > 10 mg/L) such as site B1 in our study area, $T_f \approx 1.2 \times 10^{-4}/(CG)$ is found.

6. In stratified waters characterized by a halocline, flocculation can be divided into two vertical layers separated by the halocline. Flocculation can be regarded homogeneous within each layer, but differs significantly between the two layers. This allows simplification of numerical modelling of flocculation into two layers in 3D models for typical stratified estuarine and coastal waters.
7. Single-class flocculation model such as the Winterwerp model is useful in understanding first-order flocculation processes in estuaries, especially in barotropic flows. However, models including multiple size classes to better present PSDs in the two layers divided by the halocline are needed to further understand flocculation dynamics in natural estuarine and coastal waters.

Author contributions

Conceptualization: J.R. and Y.Z.; Data curation: Y.Z.; Methodology. Y.Z. and J.R.; Modelling: Y.Z.; Investigation: J.R. and Y.Z.; Original draft: Y.Z.; Writing - review & editing: Y.Z., J.R, and W.Z.

Declaration of Competing Interest

The authors declare that they have no known competing financial interests or personal relationships that could have appeared to influence the work reported in this paper.

Acknowledgments

This work was jointly supported by National Natural Science Foundation of China (NSFC) [Grant number 41476072], and National Important Scientific Research Program of China [Grant number 2018YFC1406602]. Great thanks should go to Huan Liu, PhD, for funding the investigation and providing his help in field observations. We also thank two anonymous reviewers, whose valuable comments contributed significantly to improve this manuscript.

References

Agrawal, Y.C. and Pottsmith, H.C., 2000. Instruments for particle size and settling velocity observations in sediment transport. Marine Geology, 168(1): 89-114.

Bowers, D.G., Binding, C.E. and Ellis, K.M., 2007. Satellite remote sensing of the geographical distribution of suspended particle size in an energetic shelf sea. Estuarine, Coastal and Shelf Science, 73(3): 457-466.

Breunig, M.M., Kriegel, H.P., Ng, R.T. and Sander, J., 2000. LOF: Identifying density-based local outliers, Proc. ACM SIGMOD.

Burt, T.N., 1986. Field settling velocities of estuary muds. Estuarine cohesive sediment dynamics. Springer, Berlin.

Cross, J., Nimmo-Smith, W.A.M., Torres, R. and Hosegood, P.J., 2013. Biological controls on resuspension and the relationship between particle size and the Kolmogorov length scale in a shallow coastal sea. Marine Geology, 343(1): 29-38.

Cuthbertson, A.J.S., Dong, P. and Davies, P.A., 2010. Non-equilibrium flocculation characteristics of fine-grained sediments in grid-generated turbulent flow. Coastal Engineering, 57(4): 447-460.

Droppo, I.G., 2006. Suspended Sediment Transport – Flocculation and Particle Characteristics, Encyclopedia of Hydrological Sciences.

Droppo, I.G., Walling, D.E., Ongley, E.D., Summer, W., Klaghofer, E. and Zhang, W., 1998. Suspended sediment structure: implications for sediment and contaminant transport modelling.

Dyer, K.R., 1989. Sediment processes in estuaries: Future research requirements. Journal of Geophysical Research, 94(C10).

Eisma, D., Bernard, P., Cadée, G.C., Ittekkot, V., Kalf, J., Laane, R., Martin, J.M., Mook, W.G., Put, A.v. and Schuhmacher, T., 1991. Suspended-matter particle size in some West-European estuaries; part II: A review on floc formation and break-up. Netherlands Journal of Sea Research, 28(3): 215-220.

Fettweis, M., Francken, F., Pison, V. and Eynde, V.D., Dries, 2006. Suspended particulate matter dynamics and aggregate sizes in a high turbidity area. Marine Geology, 235(1): 63-74.

Fettweis, M., Lee, B.J., Chen, P. and Yu, J.C.S., 2012. Hydro-meteorological influences and multimodal suspended particle size distributions in the Belgian nearshore area (southern North Sea). Geo-Marine Letters, 32(2): 123-137.

Guerra, M. and Thomson, J., 2017. Turbulence measurements from five-beam acoustic doppler current profilers. Journal of Atmospheric and Oceanic Technology, 34(6): 1267-1284.

Guo, C., He, Q., Guo, L. and Winterwerp, J.C., 2017. A study of in-situ sediment flocculation in the turbidity maxima of the Yangtze Estuary. Estuarine, Coastal and Shelf Science, 191: 1-9.

Guo, C., He, Q., Van Prooijen, B.C., Guo, L., Manning, A.J. and Bass, S., 2018. Investigation of flocculation dynamics under changing hydrodynamic forcing on an intertidal mudflat. Marine Geology, 395: 120-132.

He, W., Xue, L., Gorczyca, B., Nan, J. and Shi, Z., 2018. Experimental and CFD studies of floc growth dependence on baffle width in square stirred-tank reactors for flocculation. Separation and Purification Technology, 190: 228-242.

Hill, P.S., 1998. Controls on floc size in the Sea. Oceanography, 11(2): 13–18.

Hinds, W.C., 1999. Aerosol technology properties, behavior, and measurement of airborne particles. John Wiley, New York, 464 pp.

Hussein, T., Maso, M.D., Petaja, T., Koponen, I., Paatero, P., P. Aalto, Hameri, K. and Kulmala, M., 2005. Evaluation of an automatic algorithm for fitting the particle number size distributions. Boreal Environment Research, 10(5): 337-355.

Kolmogorov, A.N., 1941. Dissipation of energy in locally isotropic turbulence. Akademiia Nauk Sssr Doklady, 32(1890): 15-17.

Kumar, R.G., Strom, K.B. and Keyvani, A., 2010. Floc properties and settling velocity of San Jacinto estuary mud under variable shear and salinity conditions. Continental Shelf Research, 30(20): 2067-2081.

Kuprenas, R., Tran, D. and Strom, K., 2018. A shear-limited flocculation model for dynamically predicting average floc size. Journal of Geophysical Research: Oceans, 123(9): 6736-6752.

Lai, H., Fang, H., Huang, L., He, G. and Danny, R., 2018. A review on sediment bioflocculation: Dynamics, influencing factors and modeling. Science of the Total Environment, 642: 1184–1200.

Lanzante, J.R., 1996. Resistant, robust and non-parametric techniques for the analysis of climate data theory and examples, including applications to historical radiosonde station data. International Journal of Climatology, 16: 1197-1226.

Lee, B.J., Fettweis, M., Toorman, E. and Molz, F.J., 2012. Multimodality of a particle size distribution of cohesive suspended particulate matters in a coastal zone. Journal of Geophysical Research: Oceans, 117(C03014).

Lee, B.J., Toorman, E. and Fettweis, M., 2014. Multimodal particle size distributions of fine-grained sediments: mathematical modeling and field investigation. Ocean Dynamics, 64(3): 429-441.

Lee, B.J., Toorman, E., Molz, F.J. and Wang, J., 2011. A two-class population balance equation yielding bimodal flocculation of marine or estuarine sediments. Water Res, 45(5): 2131-45.

Leussen, W.V., 1999. The variability of settling velocities of suspended fine-grained sediment in the Ems estuary. Journal of Sea Research, 41(1-2): 0-118.

Li, D., Li, Y. and Xu, Y., 2017. Observations of distribution and flocculation of suspended particulate matter in the Minjiang River Estuary, China. Marine Geology, 387: 31-44.

Maggi, F., 2009. Biological flocculation of suspended particles in nutrient-rich aqueous ecosystems. Journal of Hydrology, 376(1): 116-125.

Maggi, F., 2013. Biological flocculation of suspended particles in nutrient-rich aqueous ecosystems. Journal of Hydrology, 376(1-2): 116-125.

Maggi, F., Mietta, F. and Winterwerp, J.C., 2007. Effect of variable fractal dimension on the floc size distribution of suspended cohesive sediment. Journal of Hydrology, 343(1-2): 43-55.

Maggi, F., Winterwerp, J.C., Fontijn, H.L., Van Kesteren, W.G.M. and Cornelisse, J.M., 2002. A settling column for turbulence-induced flocculation of cohesive sediments, Hydraulic Measurements & Experimental Methods Specialty Conference.

Mäkelä, J.M., Koponen, I.K., Aalto, P. and Kulmala, M., 2000. One-year data of submicron size modes of tropospheric background aerosol in Southern Finland. Journal of Aerosol

Science, 31(5): 595-611.

Manning, A.J. and Dyer, K.R., 1999. A laboratory examination of floc characteristics with regard to turbulent shearing. Marine Geology, 160(1): 147-170.

Mietta, F., Chassagne, C., Manning, A.J. and Winterwerp, J.C., 2009. Influence of shear rate, organic matter content, pH and salinity on mud flocculation. Ocean Dynamics, 59(5): 751-763.

Mikkelsen, O. and Pejrup, M., 2001. The use of a LISST-100 laser particle sizer for in-situ estimates of floc size, density and settling velocity. Geo-Marine Letters, 20(4): 187-195.

Nguyen, T.H., H.M., T.F. and Federico, M., 2018. Micro food web networks on suspended sediment. Science of The Total Environment, 643: 1387-1399.

Olyaie, E., Banejad, H., Chau, K.-W. and Melesse, A.M., 2015. A comparison of various artificial intelligence approaches performance for estimating suspended sediment load of river systems: a case study in United States. Environmental Monitoring Assessment, 187(4): 189.

Pope, S.B., 2000. Turbulent flows. Cambridge University Press, 802 pp.

Ren, J. and Wu, J., 2014. Sediment trapping by haloclines of a river plume in the Pearl River Estuary. Continental Shelf Research, 82: 1-8.

Sahin, C., 2014. Investigation of the variability of floc sizes on the Louisiana Shelf using acoustic estimates of cohesive sediment properties. Marine Geology, 353(4): 55-64.

Shamshirband, S., Nodoushan, E.J., Adolf, J.E., Manaf, A.A., Mosavi, A. and Chau, K.-w., 2019. Ensemble models with uncertainty analysis for multi-day ahead forecasting of chlorophyll a concentration in coastal waters. Engineering Applications of Computational Fluid Mechanics, 13(1): 91-101.

Shen, X., Lee, B.J., Fettweis, M. and Toorman, E.A., 2018a. A tri-modal flocculation model coupled with TELEMAC for estuarine muds both in the laboratory and in the field. Water Research, 145: 473-486.

Shen, X. and Maa, J.P.Y., 2015. Modeling floc size distribution of suspended cohesive sediments using quadrature method of moments. Marine Geology, 359: 106-119.

Shen, X. and Maa, J.P.Y., 2016. Numerical simulations of particle size distributions: Comparison with analytical solutions and kaolinite flocculation experiments. Marine Geology, 379: 84-99.

Shen, X., Toorman, E.A., Joon Lee, B. and Fettweis, M., 2018b. Biophysical flocculation of suspended particulate matters in Belgian coastal zones. Journal of Hydrology, 567: 238–252.

Shen, X., Toorman, E.A., Lee, B.J. and Fettweis, M., 2018c. An approach to modeling biofilm growth during the flocculation of suspended cohesive sediments. Journal of Geophysical Research: Oceans, 124: 4098–4116.

Sreenivasan, K.R., 1995. On the universality of the kolmogorov constant. Physics of Fluids, 7(11): 2778-2784.

Thomas., D.N., Judd., S.J. and Fawcett., N., 1999. Flocculation Modelling: A Review. Water Res.

Thompson, R., 1985. A note on restricted maximum likelihood estimation with an alternative outlier model. Journal of the Royal Statistical Society. Series B (Methodological), 47(1): 53-55.

Tran, D., Kuprenas, R. and Strom, K., 2018. How do changes in suspended sediment concentration alone influence the size of mud flocs under steady turbulent shearing? Continental Shelf Research, 158: 1-14.

van Leussen, W., 1994. Estuarine macroflocs and their role in fine-grained sediment transport. PhD dissertation Thesis.

Whitey, K., 2007. The physical characteristics of sulfur aerosols. Atmospheric Environment, 41: 25-49.

Winterwerp, J.C., 1998. A simple model for turbulence induced flocculation of cohesive sediment. Journal of Hydraulic Research, 36(3): 309-326.

Winterwerp, J.C., 2002. On the flocculation and settling velocity of estuarine mud. Continental Shelf Research, 22(9): 1339-1360.

Winterwerp, J.C. and Kesteren, W.G.M.V., 2004. Introduction to the physics of cohesive sediment in the marine environment. Delft Hydraulics & Delft University of Technology, Delft, Netherlands.

Zhang, G., Cheng, W., Chen, L., Zhang, H. and Gong, W., 2019a. Transport of riverine sediment from different outlets in the Pearl River Estuary during the wet season. Marine Geology, 415: 105957.

Zhang, J., Shen, X., Zhang, Q., Maa, J.P.Y. and Qiao, G., 2019b. Bimodal particle size distributions of fine-grained cohesive sediments in a settling column with oscillating grids. Continental Shelf Research, 174: 85-94.

Zhang, J., Zhang, Q., Maa, P.Y. and Qiao, G., 2013. Lattice Boltzmann simulation of turbulence-induced flocculation of cohesive sediment. Ocean Dynamics, 63(9-10): 1123-1135.

Figure 1
Click here to download high resolution image

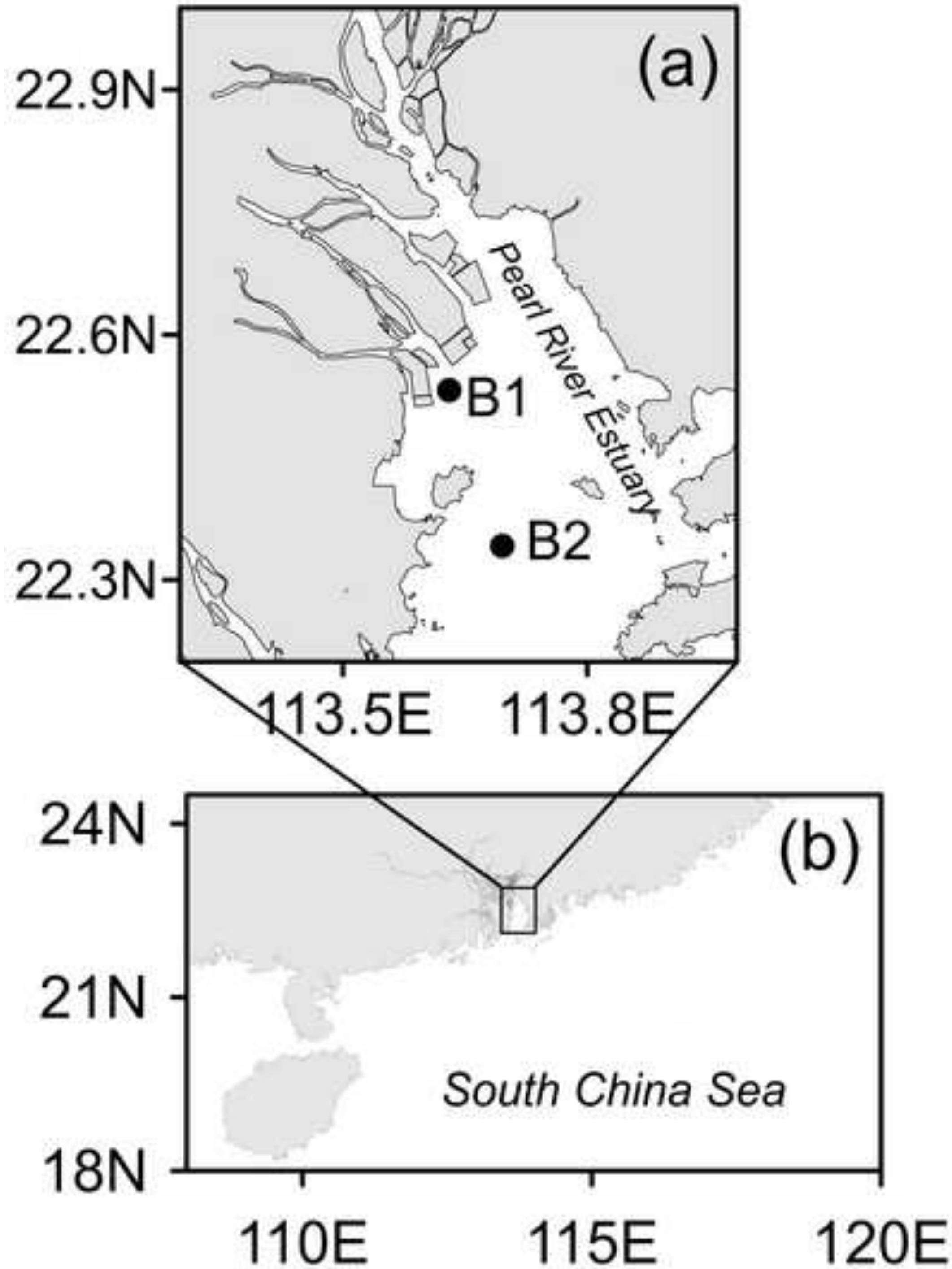

Figure 2

Click here to download high resolution image

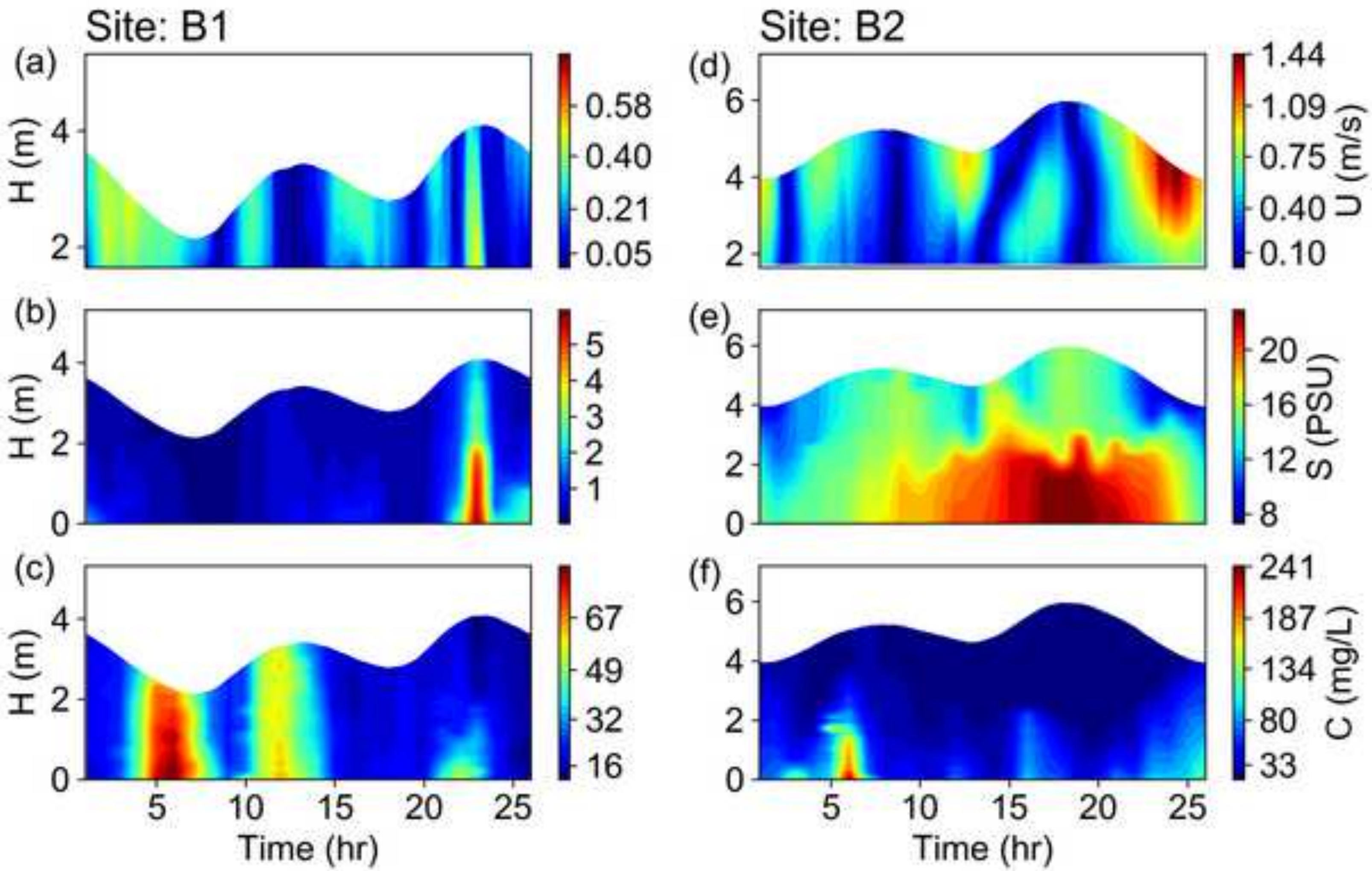

Figure 3

Click here to download high resolution image

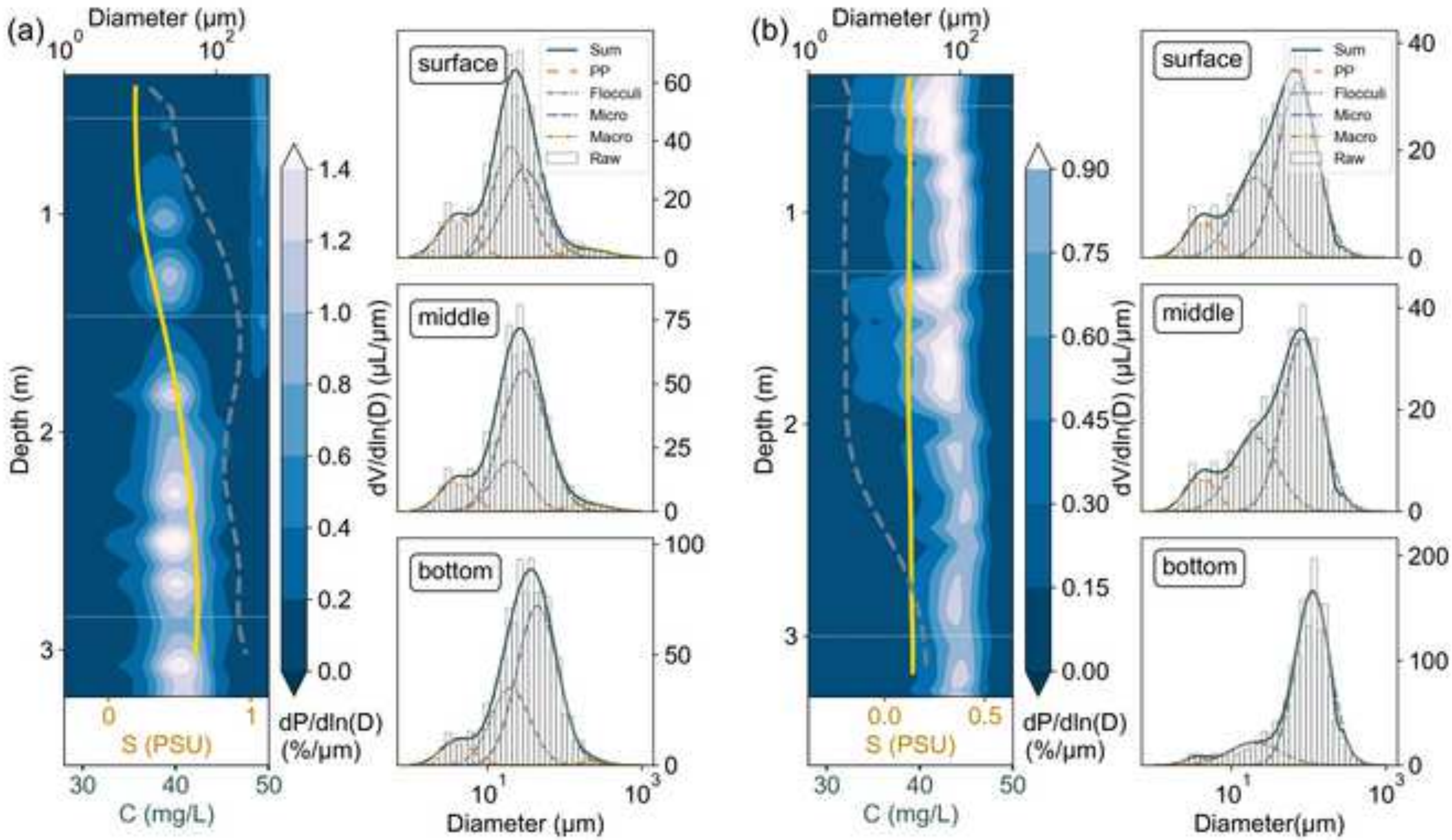

Figure 4
Click here to download high resolution image

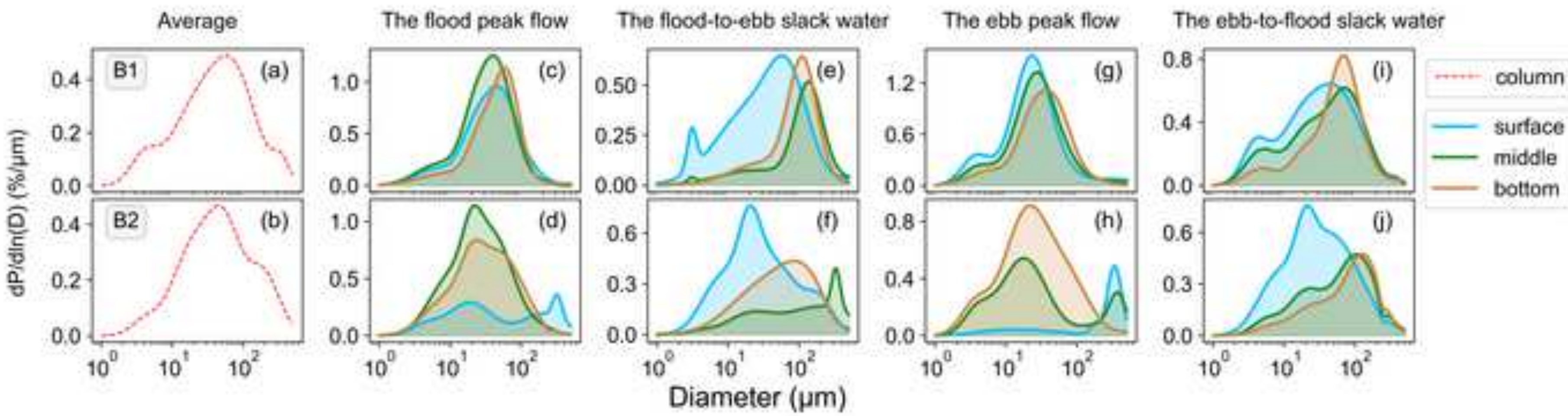

Figure 5
Click here to download high resolution image

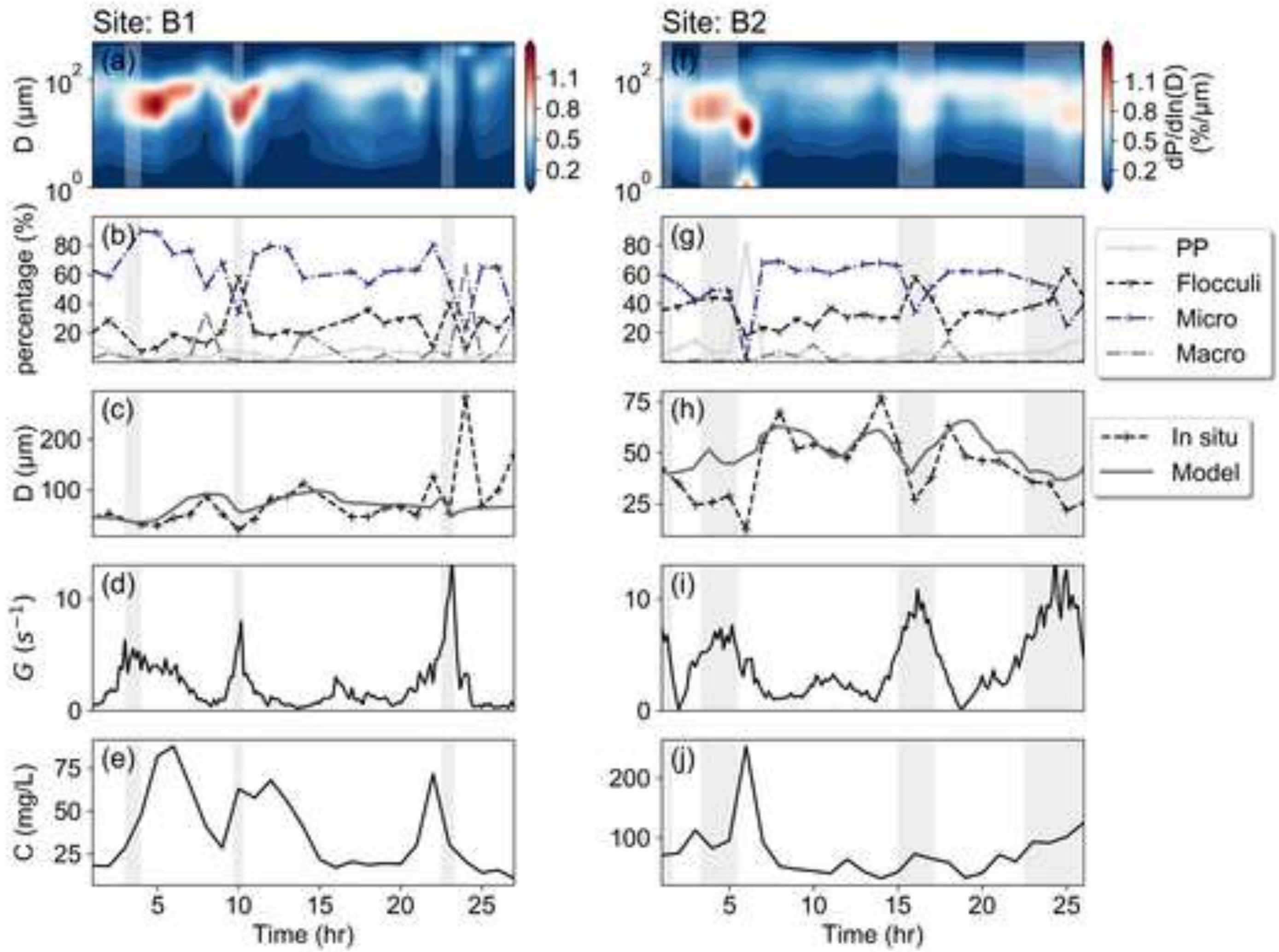

Figure 6

Click here to download high resolution image

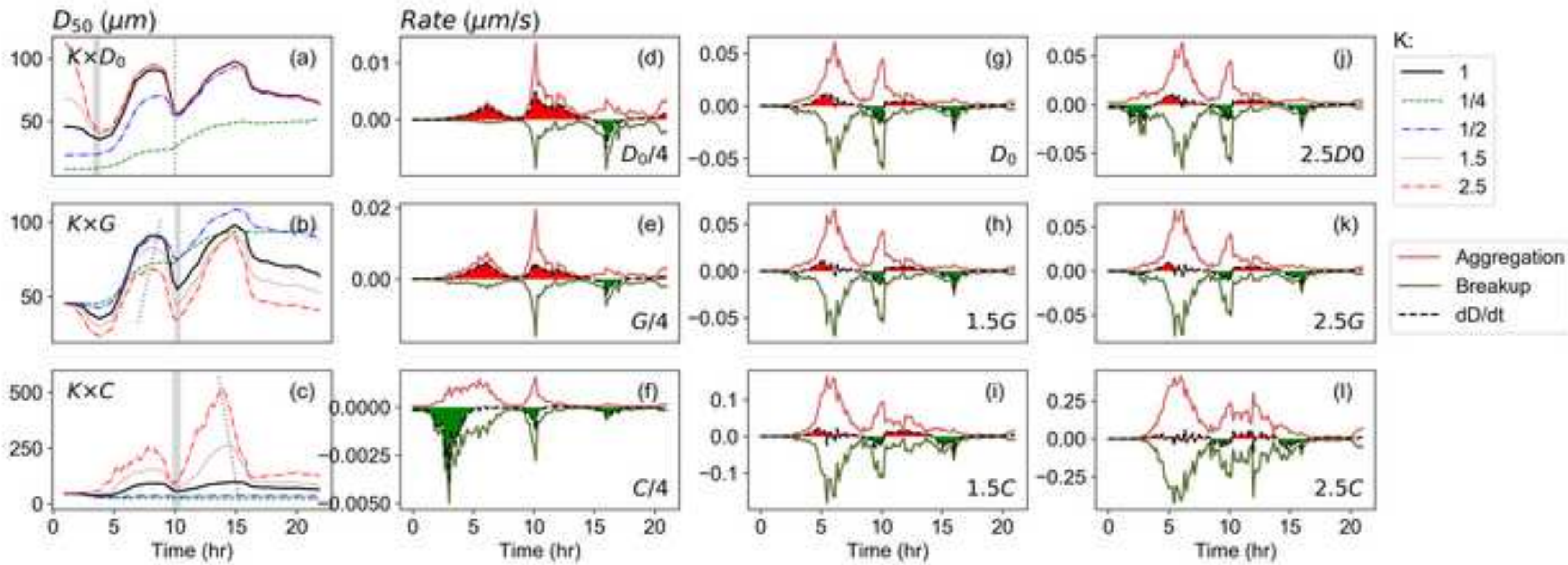

Figure 7
Click here to download high resolution image

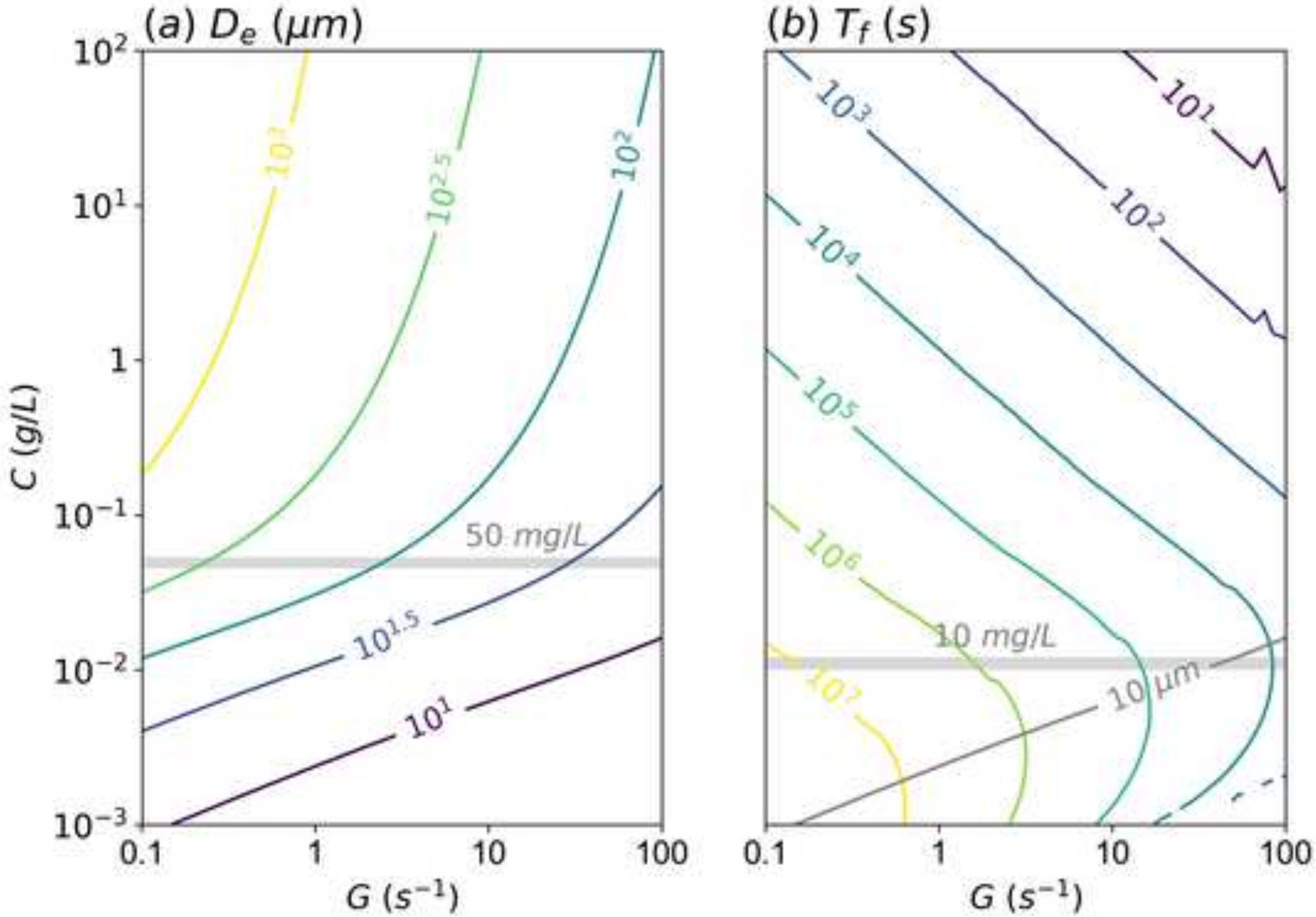

Figure 8

Click here to download high resolution image

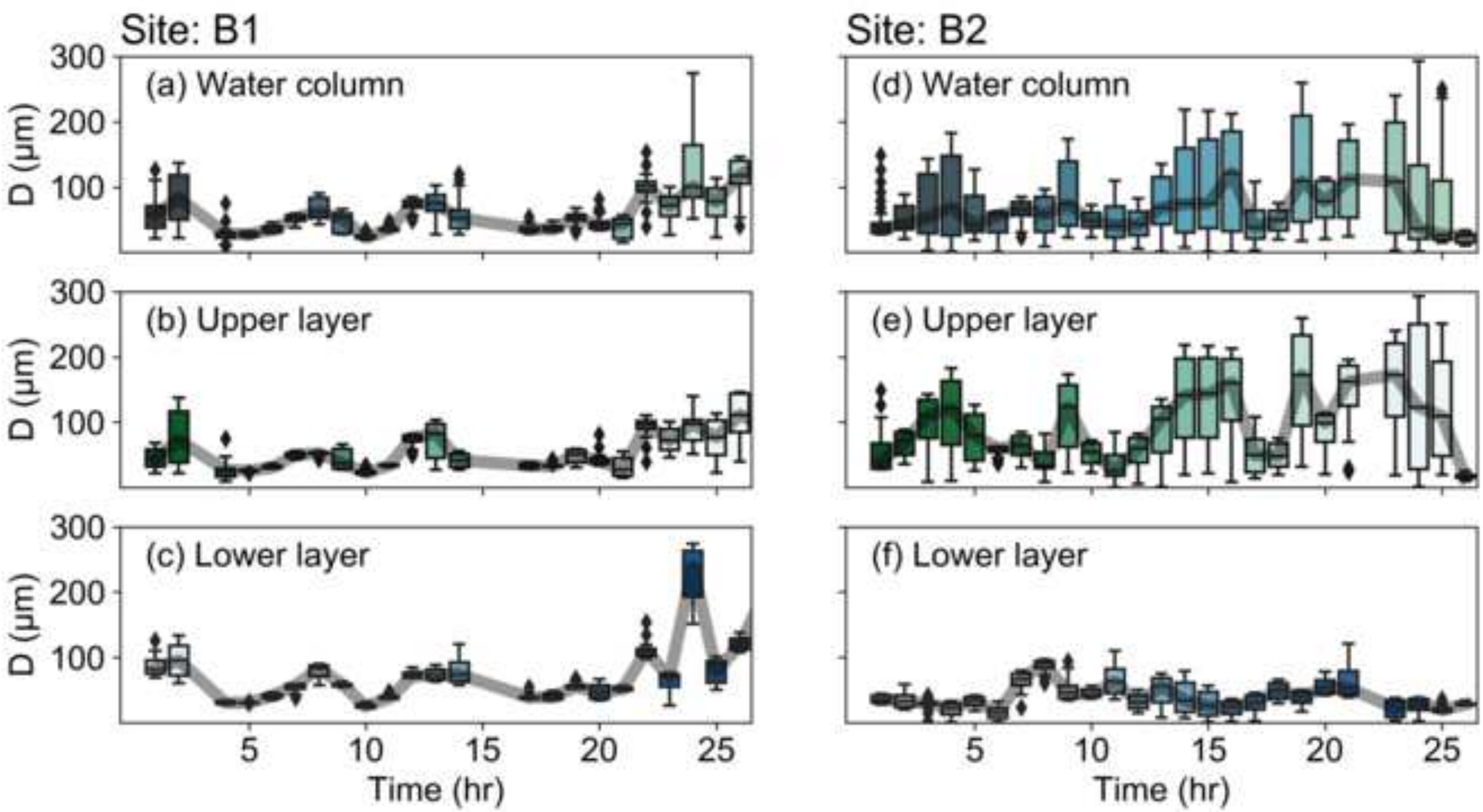

Figure Captions

Fig. 1 Locations of (a) the field survey sites and (b) the study area of the Pearl River Estuary.

Fig. 2 Times series of (a) and (d) velocity (m/s), (b) and (e) salinity (PSU), and (c) and (f) suspended sediment concentration (mg/L) at site B1 (left panels) and site B2 (right panels).

Fig. 3 Normalized PSDs (contour maps), salinity (yellow solid lines), and concentration (gray dotted lines) in the vertical and the PSDs in the surface, middle, and bottom layers under (a) high and (b) low turbulent shear with similar salinity structure. Here, and represent the volumetric and volumetric percentage normalized by the width of the size interval in the log scale, respectively, in accordance with the lognormal distribution function. PP, Flocculi, Micro, Macro, Sum, and Raw represent the decomposed PSDs of primary particles, flocculi, microflocs, and macroflocs, the superposition of the decomposed PSDs, and the PSDs measured with the LISST instrument, respectively.

Fig. 4 Normalized measured PSDs in the whole water column (red dashed lines) or surface (blue lines), middle (green lines), and bottom (brown lines) layers: (a) and (b) tidal averages and (c)–(j) characteristic moments. (c) and (d) present the flood peak flow, (e) and (f) show the flood to ebb slack water, (g) and (h) present the ebb peak flow, and (i) and (j) show the ebb to flood slack water during the tidal cycle at site B1 (upper panels) and B2 (lower panels). Here, is the volumetric percentage normalized by the width of the size interval in the log scale.

Fig. 5 Times series of (a) and (f) normalized PSDs of the bottom layer, (b) and (g) volumetric percentage of primary particles (PP), Flocculi, microflocs (Micro), and macroflocs (Macro), (c) and (h) measured (dashed lines) and simulated (solid lines) mean floc diameter, (d) and (i) turbulent shear rate, and (e) and (j) suspended sediment concentration at site B1 (left panels) and B2 (right panels). Here, $dP/dln\,(D)$ is the volumetric percentage normalized by the width of the size interval in the log scale. A grey area in (c)–(j) indicates $G > 5$/s.

Fig. 6 Time series of modeled floc diameter, aggregation, breakup, and net flocculation rate: multiplied by (a), (d), (g), and (j) initial particle diameter, (b), (e), (h), and (k) turbulent shear rate, and (c), (f), (i), and (l) sediment concentration with factors of K based on site B1 data. All other parameters are set to the values modeled at site B1.

Fig. 7 (a) Equilibrium diameter (D_e) and (b) flocculation time (T_f) under different rates of turbulent shear and sediment concentration conditions. All other parameters are set to the values modeled at site B1.

Fig. 8 Times series of measured particle size in the (a) and (d) whole water column, (b) and (e) upper layer, and (c) and (f) lower layers at site B1 (left panels) and site B2 (right panels).